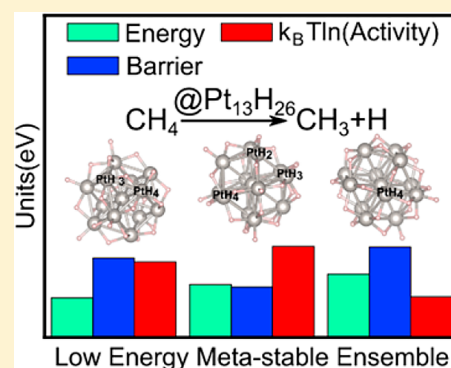


Metastable Structures in Cluster Catalysis from First-Principles: Structural Ensemble in Reaction Conditions and Metastability Triggered Reactivity

Geng Sun[†] and Philippe Sautet^{*,†,‡,§}[†]Department of Chemical and Biomolecular Engineering, University of California, Los Angeles, Los Angeles, California 90095, United States[‡]Department of Chemistry and Biochemistry, University of California, Los Angeles, Los Angeles, California 90095, United States

S Supporting Information

ABSTRACT: Reactivity studies on catalytic transition metal clusters are usually performed on a single global minimum structure. With the example of a Pt₁₃ cluster under a pressure of hydrogen, we show from first-principle calculations that low energy metastable structures of the cluster can play a major role for catalytic reactivity and that hence consideration of the global minimum structure alone can severely underestimate the activity. The catalyst is fluxional with an ensemble of metastable structures energetically accessible at reaction conditions. A modified genetic algorithm is proposed to comprehensively search for the low energy metastable ensemble (LEME) structures instead of merely the global minimum structure. In order to reduce the computational cost of density functional calculations, a high dimensional neural network potential is employed to accelerate the exploration. The presence and influence of LEME structures during catalysis is discussed by the example of H covered Pt₁₃ clusters for two reactions of major importance: hydrogen evolution reaction and methane activation. The results demonstrate that although the number of accessible metastable structures is reduced under reaction condition for Pt₁₃ clusters, these metastable structures can exhibit high activity and dominate the observed activity due to their unique electronic or structural properties. This underlines the necessity of thoroughly exploring the LEME structures in catalysis simulations. The approach enables one to systematically address the impact of isomers in catalysis studies, taking into account the high adsorbate coverage induced by reaction conditions.



1. INTRODUCTION

The determination of the structure of heterogeneous catalytic systems, under reaction conditions, is a key point for a detailed understanding of the nature of active sites and for the rational design of efficient catalysts. Theoretical simulations have been very successful to provide insight on catalysts and catalyzed reactions in the past decades, and played a key role to rationally design new catalysts.¹ Computational chemistry can address the atomic-level structure of the catalytic active site, which is the prerequisite for catalysis study, and is difficult to extract from experiment results alone. For modeling studies, catalyst structures can be manually initiated from chemical intuition, but this is not reliable for large systems that might present an important number of local minima. In addition, the catalyst structures can be profoundly altered during the reaction, following the adsorption of reactants and formation of stable reaction intermediates. Resolving the catalyst structures at reaction atmosphere is still a great challenge for modern experimental methods. Alternatively, catalyst structures can be predicted from first-principles based global optimization methods like genetic algorithm (GA),^{2–7} basin-hopping (BH),⁸ particle-swarm optimization (PSO),⁹ coalescence

kick^{10,11} etc. As long as we know some primary information like the elements in the system and reaction conditions (temperatures and pressures), it is in principle feasible to predict the equilibrium state of any catalyst structures with the help of first-principles thermodynamics.^{12,13}

Nevertheless, although global optimizations could reliably produce a putative global minimum structure at given conditions, the scenario is more complicated for catalysis because researchers are also concerned about the relevance of the predicted structure for catalytic reactivity. The low energy structures have the larger occurrence probability at finite temperatures,¹⁴ but that does not ensure that the global minimum structure is the most accountable for the observed activity. Metastable isomers of the catalyst are not as stable as global minimum but may lead to higher activity. For example, *hcp* Co(0001) terrace is more stable than other step sites, but they do not represent the most productive site for CO dissociations.¹⁵ Contributions of different surfaces can be normalized by Wulff construction¹⁶ and the results show that

Received: October 21, 2017

Published: February 9, 2018



Co(11–21) surface, who has a higher surface energy ($\gamma = 163 \text{ meV}/\text{\AA}^2$) and a smaller contribution to the nanoparticle surface, still contributes the major part of CO dissociation reactions. Another example concerns single site Mo catalyst on γ -alumina for metathesis catalysis. We showed earlier that the catalytically relevant sites do not correspond to the lowest-energy configuration for Mo species, and that hence only a small fraction of the surface Mo sites are active.¹⁷ A similar study was conducted on amorphous alumina by Goldsmith et al.¹⁸ Very recently, Alexandrova and co-workers showed that the statistical ensemble of isomers of a Pt₇ cluster supported on alumina should be considered for the dehydrogenation of ethene in ultrahigh vacuum.^{19–21} The above examples show that it is incorrect to neglect metastable structures in catalysis studies. Experimental characterization of metastable/minority structures is very challenging since spectroscopic methods probe the average state of the system. Therefore, efficient computational methods to systematically search for low energy isomers instead of merely global minimum are essential for understanding and design of catalysts. One of the aims of the current work is to develop and validate a modified global optimization method to search for low energy isomers along with the global minimum structure.

Beyond developing an algorithm for locating catalyst (metastable) structures, there is still a large challenge because first-principles calculations are too CPU intensive. In all the global optimization algorithms, a large number of local optimizations are needed in order to reduce the total effective configuration space.²² Since the computational cost of density functional theory (DFT) grows cubically with the size of the system and the configuration space also grows exponentially with the number of atoms, the global optimization with pure DFT calculations for larger system is not accessible. In order to circumvent the expensive DFT calculations, one can use empirical force fields. One option is called reactive force field, which uses bond orders to describe the interactions between atoms. The most popular implementation of the reactive force field is ReaxFF,^{23,24} which can be used for many heterogeneous materials but the transferability and accuracy are not always satisfactory. The second option is based on statistical learning techniques, also called machine learning force field (MLFF). MLFF predicts the energies and forces according to a statistical learning of the model and an interpolation between reference structures and new structures. On the basis of different mathematical models, some promising MLFF are actively developed including GAP (Gaussian Approximation Potential)²⁵ or NNP (Neural Network Potential),^{26–32} Compared with ReaxFF that exploits fixed physical models, MLFF are in principle more flexible and can be fitted to arbitrarily complex interactions. In this work, we are taking advantage of a high dimensional neural network potential (HDNNP)^{26–33} to accelerate the global optimization. These HDNNP are based on atomic energy contributions and can be applied to systems of large size. They go beyond the limitations of previous neural networks for fixed-size systems. Some previous works have exploited HDNNP to study interface structures, supported metal clusters, metallic alloys etc. and the results demonstrate the applicability of HDNNP in a wide range of materials.³⁴

A platinum subnanocluster (Pt₁₃) submitted to a pressure of hydrogen, and hence covered with hydrogen adatoms, is used here as an example to demonstrate the fluxional nature of the cluster catalyst, the large size of the LEME, the influence of hydrogen coverage (controlled by the hydrogen pressure and

the temperature) and the key role of metastable structures in catalytic reactivity. This is enabled by the combination of a modified genetic algorithm (MGA) and a DFT trained HDNNP potential. Pt clusters are chosen because of their high importance in industrial processes as alkane dehydrogenation, water–gas shift, CO oxidation, hydrogen evolution reaction (HER), etc.^{35–40} Therefore, they have attracted a large effort from both experiment studies and theoretical simulations.^{2,41–43} More specifically we will consider here HER and methane activation as reaction examples. This manuscript is organized as follows: section 3 describes the simulations and the proposed MGA method, which can be used for efficient searching of the low energy metastable ensemble (LEME) structures; section 4 shows the LEME structures for the bare and hydrogen covered Pt₁₃ cluster; and section 5 shows the role of metastable structure for the hydrogen evolution and methane activation reactions.

2. COMPUTATIONAL DETAILS

2.1. Training a High Dimensional Neural Network Potential for Pt_nH_x Clusters. In order to reduce the total computational cost during structure exploration, and make extensive configuration search possible for systems containing up to 39 atoms, we are exploiting HDNNP to describe the interatomic potentials in Pt_nH_x systems. The details and advantages of HDNNP are described in other papers.^{26–30,32,44} In this part, we are only briefly summarizing the basic ideas. HDNNP formulates the total energy of a system as the summation of atomic contributions, where the atomic energy is a function of its chemical environment. Therefore, atomic positions are not directly used as the input for HDNNP. Instead, coordinates are transformed by symmetry functions into a numerical array characterizing the chemical environment of each atom. There are two different types of symmetry functions, namely, radial and angular; the first one is formulated as²⁸

$$G_i^2 = \sum_{j=1}^{N_{\text{atoms}}} e^{-\eta_i(R_{ij}-R_c)^2} f(R_{ij}) \quad (1)$$

where R_{ij} is the distance between atom i and atom j , R_c is a shift parameter which can render G_i^2 more sensitive at a desired distance and $f(R_{ij})$ is a smooth cutoff function, which vanishes if R_{ij} is larger than a chosen cutoff distance R_c . Usually, the function f can take the form²⁸

$$f(R_{ij}) = \begin{cases} 0.5 \times \left[\cos\left(\frac{\pi R_{ij}}{R_c}\right) + 1 \right] & \text{if } R_{ij} < R_c \\ 0 & \text{if } R_{ij} > R_c \end{cases} \quad (2)$$

The angular symmetry function is formulated as²⁸

$$G_i^4 = 2^{1-\zeta} \sum_{j,k \neq i}^{\text{all}} (1 + \lambda \cos \theta_{ijk})^\zeta \times e^{-\eta_2(R_{ij}^2 + R_{ik}^2 + R_{jk}^2)} \times f(R_{ij})f(R_{jk})f(R_{ik}) \quad (3)$$

where θ_{ijk} is the angle between atoms i , j and k . The summation runs over all the k , j atoms pairs. There are strong advantages in using symmetry functions over Cartesian coordinates: the most important one is that the output energy of HDNNP automatically fulfills the permutation symmetry, which means that the interchange of two atoms of the same kind does not change the energy of the system. The second one is that symmetry functions are better ways to extract the features of atomic environments than Cartesian coordinates.⁴⁵ The third one is that due to the assumption that total energy is the summation of atomic energies, the HDNNP is naturally suitable for systems with variable composition and size, which is of significant importance for catalysis studies, and is key for our study. The NN

training process for this work is described in details in the [Supporting Information](#) (Section S3).

2.2. Modified Genetic Algorithm (MGA) for Low Energy Metastable Ensemble. The low energy metastable ensemble (LEME) can be precisely defined as all the structures, whose energy lie between the global minimum E_{gm} and $E_{\text{gm}} + E_{\text{window}}$. In order to search LEME structures, a highly efficient algorithm is vital to reduce the total computational cost and get reliable results. The proposed algorithm should have the following features: (1) The algorithm should focus on sampling the low energy configurations. Because the number of structures grows exponentially with increasing potential energy, it is impossible to enumerate all the local minima before selecting LEME. (2) The algorithm should be also efficient to achieve the global minimum simultaneously along with the exploration of LEME. Before the exploration, we have no idea about the global minimum structure, so we also do not know which energy range is relevant for the definition of the LEME. According to those standards, there are many global optimization algorithms that may be applicable to search for the LEME, and here we chose the genetic algorithm and improve it for our purpose. Wales et al. also proposed an approach to search for low energy structures,⁴⁶ but their method requires a vast number of structure optimizations, transition state searching and Hessian eigenvalue evaluations. Their method is more suitable for studies based on empirical potentials like Lennard-Jones clusters rather than first-principles calculations.

Like other global optimization algorithms, normal GA is used for generating the global minimum structure. The metastable structures generated during the exploration are only “by-products”, hence there is no indicator to know the credibility and completeness of the LEME structures from normal GA. We are solving this problem by designing a new termination threshold for a MGA approach, which employs a single parameter N_{wait} to control the reliability of the acquired LEME. Increasing the value of N_{wait} can systematically improve the confidence in the completeness of the LEME. The details of MGA are given in the [Supporting Information](#) (Section S4). We also validated our proposed MGA approach by searching the LEME for a model Lennard-Jones cluster (LJ_{38}), and the results demonstrated the efficiency and reliability of this approach over the random exploration method (see [Figure S4](#)).

Another mandatory effort in this proposed approach is to alleviate the intensive computational cost of first-principles calculations, therefore, we exploit HDNNP potential to preoptimize structures in GA, which are far away from the local minima. Before optimization by DFT calculations, using HDNNP potentials to filter out the unreasonable structures and to drive all initial structures into a more reasonable geometry strongly accelerate the exploration, and make it accessible. The cooperation between HDNNP on MGA explorations is described in [Supporting Information](#) section S4.1.

MGA explorations are initially performed using the PBE functional for the DFT calculations. After MGA optimizations, all the structures in the LEME are reoptimized with the optPBE-vdW functional, more expensive but more accurate for both Pt–H interaction and Pt cohesive energy.^{47,48} Some newly proposed functionals also show a good accuracy for the Pt–H system,⁴⁹ but extensive testing of new functionals is beyond our current scope. We checked that changes in the stability order between isomers when going from PBE to optPBE-vdW only affects high energy isomers, and has no influence on our conclusions.

3. RESULTS AND DISCUSSION

3.1. MGA Exploration of Structures of Pt_{13} , $\text{Pt}_{13}\text{H}_{18}$, and $\text{Pt}_{13}\text{H}_{26}$. MGA explorations of Pt_{13}H_x are conducted with three different amount of H atoms x ($x = 0, 18, 26$, respectively). The final size of the structure pool in MGA explorations and the number of structures in LEME are listed in Table S4 in the [SI](#).

LEME Structures of Pt_{13} . For Pt_{13} there are in total 49 structures in the 0.5 eV interval from the global minimum. Their relative energies (using the global minimum energy as

reference) and the structures of the three most stable ones are shown in [Figure 1](#). All the other structures in the LEME of Pt_{13}

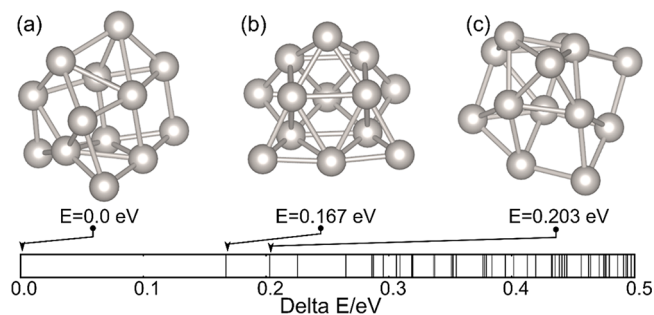


Figure 1. Relative energies (eV) of the 49 Pt_{13} isomers in the LEME (zero represents the energy of the global minimum) and structures of the three most stable ones.

are given in [Figure S5](#). The first metastable isomer is 0.167 eV above the global minimum and then the density of isomer increases with energy, which is similar to the potential energy surfaces of Lennard-Jones clusters as shown by the disconnectivity graph used by Wales et al.⁴⁶ This observation also shows that it may be difficult to use too large E_{window} in the MGA exploration. Fortunately, for many practical cases, there is only a limited number of isomers which are thermodynamically accessible and they can be explored by the proposed MGA method.

As shown in [Figure 1\(a\)](#), the global minimum of Pt_{13} is not a bulk truncated cuboctahedron structure or other high symmetry topology,⁵⁰ but a low symmetry structure which is designated as a tricapped pentagonal prism structure by Zhai et al.⁵¹ or disordered structure (DIS) by Bunău et al.⁵² The global minimum structure shows a mirror symmetry, which is also reported in other first-principles calculations.^{51,53} The average coordination number of the Pt_{13} global minimum is 4.2 and this is smaller than that of the most compact cuboctahedron structure ($\text{CN}(\text{average}) = 5.5$), which indicates that the coordination number is not the only factor influencing cluster stability. Pt has an almost full 5d shell, so that d–d interaction between neighboring Pt atoms are destabilizing, explaining why stability does not improve necessary with increased coordination.⁵⁴ The markedly lower coordination in Pt_{13} compared to the bulk clearly results in shorter Pt–Pt bond lengths and a stronger Pt–Pt interaction. The first metastable structure is more symmetric. The coordination numbers of Pt atoms in the cluster are detailed in [Figure S10](#). It shows that the maximum Pt–Pt coordination number is 8 in the LEME structures, and some LEME structures have Pt atoms with a coordination as low as 2. It should be noted that the regular high symmetry cuboctahedron structure has a high energy (3.316 eV) and is by far not among the LEME structures. Spin–orbit coupling (SOC) might have an effect on the relative energy of small Pt clusters.^{55,56} We have recalculated the 15 most stable Pt_{13} structures including SOC (see [Figure S12](#) in [SI](#)) using a PBE-based approximation scheme (eq S12). Relative energies of the various isomers are only affected by 0.1–0.2 eV. Nevertheless, an accurate evaluation of the energy difference between Pt_{13} cluster isomers requires SOC calculations. The hydrogenated clusters considered further are calculated with the optPBE-vdW functional and SOC effects are not included.

Structures of $\text{Pt}_{13}\text{H}_{18}$. The LEME of $\text{Pt}_{13}\text{H}_{18}$ contains 20 isomers. Their energies and the structures of the three most

stable ones are shown in Figure 2, while all 20 geometries are shown in Figure S6. There is no magnetization density for all

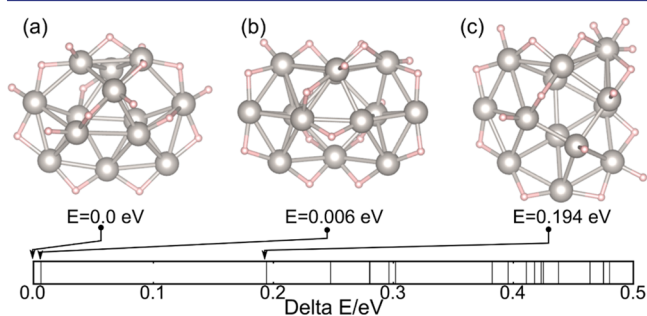


Figure 2. Relative energies (eV) of the 20 $\text{Pt}_{13}\text{H}_{18}$ isomers in the LEME (zero represents the energy of the global minimum) and structures of the three most stable ones. Small balls are H atoms and large balls are Pt atoms. The structures are shown in the direction where different layers are “stacked” (see main text).

the LEME structures of $\text{Pt}_{13}\text{H}_{18}$. The smaller number of LEME structures (20 vs 49) demonstrates a slightly more rigid cluster upon H adsorption. It should be underlined that the structures of the Pt_{13} cores in the 20 LEME structures of $\text{Pt}_{13}\text{H}_{18}$ are all topologically different from the 49 LEME structures of Pt_{13} . H adsorption hence deeply modifies the structure of the Pt_{13} core and does not only produce a limited relaxation of the Pt_{13} geometries. Similar with the Pt_{13} series, none of the 20 LEME structures exhibit the cuboctahedron Pt_{13} frame. The two lowest energy structures are very close in energy (by 0.006 eV) and both of them show a seashell like geometry. There are 7 Pt atoms forming a 7-membered ring and rest of the Pt atoms are located on both sides of the ring. The third lowest minimum has a significantly higher energy (0.194 eV). Though the Pt frame and H positions in $\text{Pt}_{13}\text{H}_{18}$ structure are quite diverse, it still can be discerned that the $\text{Pt}_{13}\text{H}_{18}$ LEME structures exhibit a disk feature, where all the atoms are arranged in approximate 2 or 3 layers and the interlayer space in the stacked direction is shorter than that of bulk. The oblate feature of the $\text{Pt}_{13}\text{H}_{18}$ clusters can be discerned from the anisotropy of the atom distribution, which is shown in Figure S13. H atoms mainly occupy top or bridge sites at the surface of the cluster (Figure 2 and S8). There are only a few hollow sites H atoms which only appear in the high energy isomers. This is very different from the H/Pt(111) structures, where H atoms favor the hollow sites. H atom do not penetrate in the interior of the cluster.

$\text{Pt}_{13}\text{H}_{26}$ Structures. There are 19 structures in the LEME for the high H coverage $\text{Pt}_{13}\text{H}_{26}$ cluster and three of them all are shown in Figure 3. There is no magnetization density for all LEME structures of $\text{Pt}_{13}\text{H}_{26}$ clusters. A major difference with the lower coverage situations is that all LEME structures exhibit a cuboctahedral Pt_{13} core and differ only by the positions of H atoms. The presence of a high coverage of H hence locks the Pt_{13} core in a unique, bulk-like geometry and completely shuffles the relative energies of the Pt structures (by more than 3 eV!). The energy of the first noncuboctahedral Pt_{13} core $\text{Pt}_{13}\text{H}_{26}$ cluster in the MGA database is 1.631 eV higher than the global minimum structure, and these structures show a *hcp* stacking rather than the *fcc* stacking in the cuboctahedron. Generally speaking, the bridge site is favored for H adsorption on cuboctahedral Pt_{13} , but it is interesting that not all the bridge sites are occupied. Instead, the global minimum structure has 6 top H atoms, which is more than the allowed minimum

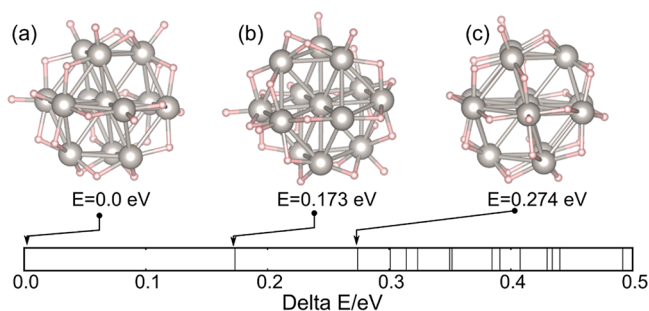


Figure 3. Relative energies (eV) of the 19 $\text{Pt}_{13}\text{H}_{26}$ isomers in the LEME (zero represents the energy of the global minimum) and structures of the three most stable ones. Big balls are Pt and small balls H atoms.

number of 2. (There are 24 edges for cuboctahedron structures, so that 4 bridge sites are vacant in the global minimum). Other structures in the LEME also favor the bridge sites and no hollow sites H atoms are observed (Figure S9). Mager-Mauray et al.⁴² also reported a stable structure of $\text{Pt}_{13}\text{H}_{26}$ with a cuboctahedron Pt_{13} inner core by molecular dynamics. This $\text{Pt}_{13}\text{H}_{26}$ structure, which has only 2 top sites H atoms and all the bridge sites on the surface of the Pt_{13} core occupied, is also found in our work and appears 0.301 eV higher than our global minimum structure.

Bond Lengths and Coordination Analysis. In order to analyze the effect of H adsorption on the reconstruction of Pt clusters, the bond lengths of first-neighbor Pt–Pt pairs and number of Pt–Pt neighbors are calculated and illustrated in Figure 4. It is clear that all the Pt–Pt distances are compressed compared with bulk Pt metals. The Pt_{13} clusters have the shortest average Pt–Pt bond distances, which only slightly vary within different metastable structures in the LEME. The average Pt–Pt bond lengths of $\text{Pt}_{13}\text{H}_{18}$ are larger than Pt_{13} and according to the colored shade, where the green shade moves up as a whole compared with the red shade, $\text{Pt}_{13}\text{H}_{18}$ clusters are slightly expanded (Figure 4(a)). This results agree well with recent work from Hiroyuki et al.⁵⁷ They studied the Pt–Pt bond lengths of sub nanoparticles as small as Pt_{4-5} and they verified the contraction of Pt–Pt bond below 1 nm nanoparticles as well as the Pt–Pt bond expansion upon H_2 adsorption. Their conclusion is verified by X-ray adsorption spectrum and they explained the contraction of Pt–Pt bond comes from the surface tension of supports. Current calculation results show that the intrinsic coordination-dependent interaction between Pt atoms has significant impact on Pt–Pt bond lengths. The average Pt–Pt coordination numbers are more or less the same between Pt_{13} and $\text{Pt}_{13}\text{H}_{18}$ clusters (Figure 4(b)), however H atoms complete the Pt coordination and Pt–H interactions result in increased Pt–Pt bond lengths (Figure 4(a)), from a simple bond-order conservation principle.⁵⁸ Because of all the $\text{Pt}_{13}\text{H}_{26}$ clusters have the same Pt framework of a cuboctahedron core, the average Pt–Pt bond lengths remain the same within the LEME structures.

If we consider the average Pt–Pt bond lengths and Pt–Pt coordination numbers in all the structure pool during the exploration (Figure 4(c,d)), there is a clear trend that the higher the energy of Pt_{13}H_x cluster is, the more the Pt–Pt bonds are compressed. This decrease of the bond lengths in higher energy isomers is faster in Pt_{13} clusters compared with that of $\text{Pt}_{13}\text{H}_{18}$ and $\text{Pt}_{13}\text{H}_{26}$. $\text{Pt}_{13}\text{H}_{26}$ gives the smallest slope. In terms of the Pt_{13} clusters, since the structures with higher energy have

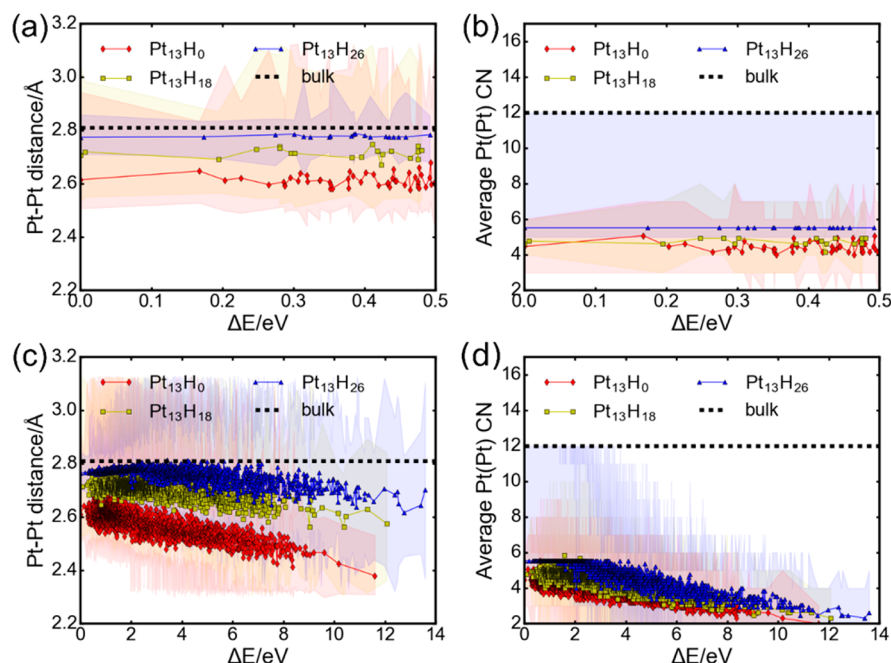


Figure 4. Structure analysis of the LEME structures using optPBE-vdw (a,b) and of all structures produced during MGA using PBE (c,d). (a) and (c) show the average bond length of first-neighbor Pt–Pt pairs, as a function of the relative energy with respect to the global minimum. The colored shade indicates the range of the Pt–Pt bond lengths. (b) and (d) illustrate the average Pt–Pt coordination numbers (CN) as well as the range of coordination numbers, where only Pt–Pt coordination is considered.

stronger bond between Pt atoms due to shorter bond lengths, the raise of the energy can be attributed to the fact that they have more open structures (lower coordination numbers). This is verified by the average Pt–Pt coordination numbers in Figure 4(d). The behavior of H covered Pt clusters is more complicated because of the involvement of H atoms, whereas it is interesting that both the bond lengths and bond coordination numbers show a similar trend compared to Pt₁₃ clusters.

3.2. First-Principles Thermodynamics Analysis of Structure Stability. In order to investigate the thermodynamic stability of the three different structures (Pt₁₃, Pt₁₃H₁₈, and Pt₁₃H₂₆) at various conditions, first-principles thermodynamics^{59,60} is exploited to study the reaction free energy of the following chemical equation:



The reaction free energy can be calculated by

$$\Delta G_r = G(\text{Pt}_{13}\text{H}_x) - \frac{x}{2}G(\text{H}_2) - G(\text{Pt}_{13}) \quad (5)$$

where $G(\text{H}_2)$ is calculated from DFT and the statistical thermodynamics of the ideal gas. $G(\text{Pt}_{13})$ and $G(\text{Pt}_{13}\text{H}_x)$ are calculated from the harmonic oscillator approximation. The resulting cluster stability diagram as a function of temperature and H₂ pressure is shown in Figure 5. It illustrates that the most stable structure (indicated by the number of H atoms) varies at different temperature and pressures. At low pressure of hydrogen and high temperature, the pure Pt₁₃ cluster is the most stable composition, which is shown in the lower right region of Figure 5 (low chemical potential of H). In contrast, the Pt₁₃H₂₆ cluster with high H coverage is preferred at higher pressure or lower temperature (high chemical potential of H). Compared with Pt₁₃H₂₆ and Pt₁₃, Pt₁₃H₁₈ is only present in a

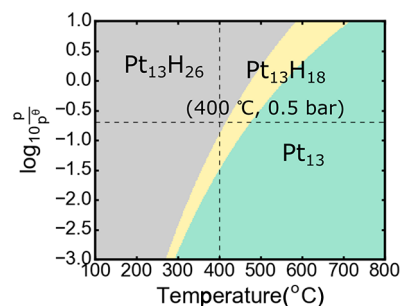


Figure 5. Thermodynamics stability of Pt₁₃H_x clusters ($x = 0, 18, 26$) as a function of temperature and hydrogen pressure. The crossing point of the dash lines indicates the assumed reaction conditions for evaluating the activity of C–H bond breaking in section 4.2.

narrow region, which is consistent with previous DFT calculation results by Mager-Maury.⁴² The above analysis is only based on the global optimization results for three H coverages of the Pt₁₃ clusters, and it obviously does not fully construct the Pt₁₃H_x stability diagram, since many other H coverage values should be considered.³⁹ It would be a very large task to determine the global minimum and LEME for all possible values of H coverage. We have hence selected typical cases of intermediate (Pt₁₃H₁₈) and high (Pt₁₃H₂₆) H coverage. Even if we did not explore the full phase diagram of Pt₁₃H_x in this work, one can conclude that a Pt₁₃ cluster shows a high coverage of H (>26, i.e., more than 2 H per Pt) in a large range of T and P. This contrasts with the Pt(111) surface that shows a max coverage of 1H per Pt. At a pressure of 1 bar, H covered clusters are stable at least until 800 K, which is significantly higher than the Pt(111) surface which becomes bare at 700 K using the same functional.⁶¹

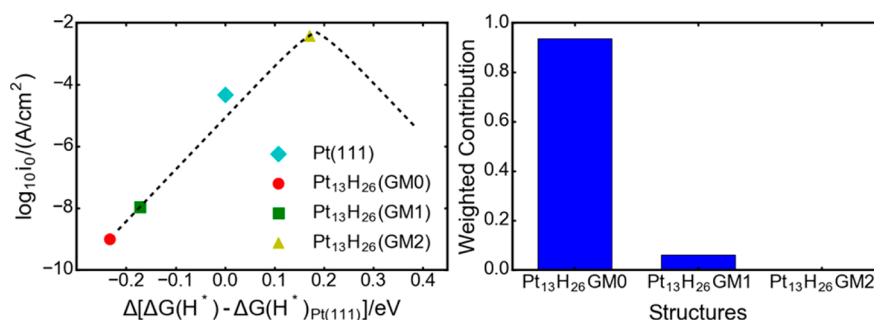


Figure 6. Activity for HER of three most stable structures of the Pt₁₃H₂₆ cluster. (left) In logarithmic scale, the exchange current densities versus the H adsorption free energies $\Delta G(H^*)$. GM0 indicates the global minimum structure of Pt₁₃H₂₆, and GM1 and GM2 are the 2nd and 3rd most-stable structures of Pt₁₃H₂₆. (right) The normalized contribution of different structures in the observed HER rate (eq 7).

4. APPLICATIONS

4.1. Pt₁₃H₂₆ Clusters in Hydrogen Evolution Reactions.

Pt is an excellent electrode material for hydrogen evolution reaction (HER), which has attracted many interests of theoretical studies to unravel the relationship between the exchange current density and electrode properties. One prevalent theory (proposed by Nørskov and co-workers)⁶² demonstrates that the binding energy of hydrogen on the metal surface (H_{ads}) can be used as the single descriptor to predict the activity of electrode material.

We will consider here the Pt₁₃ cluster as a model catalyst for HER, performed in acidic conditions. One important question is to determine the type of hydrogen coverage (low, intermediate, high) in operating HER conditions. The Pourbaix diagram, expressing the relative stability of Pt₁₃, Pt₁₃H₁₈ and Pt₁₃H₂₆ as a function of the applied electrochemical potential and of the pH (for acidic pH) is presented in the SI (Figure S16). At small negative potential, typical case for HER, the high coverage Pt₁₃H₂₆ cluster is the most stable one in acidic conditions. In this work, we are hence using the LEME structures of Pt₁₃H₂₆ as model catalysts for the HER reaction to demonstrate that both global minimum structure and metastable structures can contribute to the experimental observed reaction current.

On Pt catalysts, the H binding energy is somewhat too strong, so that weaker H adsorption is required to enhance the HER activity. We hence studied the adsorption free energy of different H atoms ($\Delta G(H^*)$) on our various LEME models. The binding energies ($\Delta E(H^*)$) for the 26 H atoms on Pt₁₃H₂₆ clusters are first calculated by removing one H atom at a time (Figure S14 and S15). The most stable structure for the Pt₁₃H₂₆ cluster is associated with the strongest interaction between H and Pt atoms and hence shows the smallest HER activity. Opposition between site stability and reactivity is frequent at catalysis studies and therefore, the fact that the stability of a catalyst and its activity do not always come together brings the necessity of also considering metastable structures. These metastable configurations are less probable, but could have a larger catalytic activity. In order to test this idea in the case of the Pt₁₃H₂₆ cluster for HER reactions, we further take into account thermodynamics corrections to evaluate the adsorption free energies ($\Delta G(H^*)$), since those entropy corrections are essential to have a more accurate prediction for the activities. In the end, the free energy of H adsorption is calculated with

$$\Delta G(H^*) = G(\text{Pt}_{13}\text{H}_{26}) - G(\text{Pt}_{13}\text{H}_{25}) - \frac{1}{2}G(\text{H}_2) \quad (6)$$

Only the weakest adsorbed H atoms are considered here to evaluate the HER reaction activity. Since the activity of HER decreases fast with increasing $|\Delta G(H^*)|$, it is justified to use the most active H to estimate the whole activity of the cluster.

The exchange current densities for the different cluster isomers are calculated with the kinetic equations derived by Nørskov and co-workers⁶² (eqs S15 and S16) and are compared with that of Pt(111) on Figure 6 ($\Delta G(H^*) = -0.18$ eV). HER activity sequence appears in the inverse order of the stability of individual clusters, the second metastable isomer being a million time more active than the global minimum. This can be explained by the generally weaker Pt–H interaction in high-energy isomers. In the end, a compromise need to be established between activity and stability and an optimum determined. In order to take both activity and stability into account, the exchange current density is weighted by the Boltzmann probability of the respective the Pt₁₃H₂₆ cluster, i.e.:

$$i_0^{\text{GMi}}(\text{eff}) = i_0^{\text{GMi}} \exp\left(-\frac{G^{\text{GMi}}(\text{Pt}_{13}\text{H}_{26}) - G^{\text{GM0}}(\text{Pt}_{13}\text{H}_{26})}{k_B T}\right) \quad (7)$$

where $G^{\text{GM0}}(\text{Pt}_{13}\text{H}_{26})$ is the free energy of the global minimum and $G^{\text{GMi}}(\text{Pt}_{13}\text{H}_{26})$ the free energy of GMi metastable structure. The normalized contribution to exchange current density is shown in Figure 6(b), while free energy values are provided in the Table S5. Figure 6 illustrates that although structure GM2 has the optimum $\Delta G(H^*)$, whose activity appears at the top of volcano curve, and hence presents a much higher activity than the global minimum structure GM0, its free energy is too high to provide a significant contribution at room temperature ($T = 298$ K). GM1 presents a much smaller activity enhancement, but it is partially populated at room temperature and shows a contribution to the total activity. In this electrocatalysis example, the population (occurrence probability) of metastable isomer is rather small compared with the global minimum because of the low reaction temperature. Nevertheless, the second most stable structure still contributes in a significant way to the total experimentally observed activity, although the global minimum dominates.

4.2. Methane Activation on Pt₁₃ and Pt₁₃H₂₆ Clusters.

As a second reaction example, we will consider light alkane dehydrogenation, a reaction with ample industrial interest for which Pt is a major catalysts and which is operated at a high temperature (360–600 °C).^{63–67} The reaction produces light alkenes, that are very important intermediates for the production of bulk chemicals and polymers. The catalyst

deactivates by coke formation and in many processes hydrogen is cofed with the alkane in order to reduce the deactivation.^{68,69} Alkane dehydrogenation can be operated at different conditions of H chemical potential: very low H chemical potential like in the work of Sattler et al.,⁷⁰ which is conducted at 600 °C, or higher H chemical potential as Biloen et al.⁷¹ with 360 °C and 2 bar H₂ for propane dehydrogenation. For this example, we will focus on the conditions where a not too high temperature is used and H₂ is cofed ($T = 400$ °C, $p(\text{H}_2) = 0.5$ bar). In such reaction conditions, our stability diagram (Figure 5) indicates that Pt₁₃H₂₆ is the most stable coverage of the Pt₁₃ particle.

We consider here the initial activation of the alkane, that we model by methane, on the bare Pt₁₃ clusters and hydrogen covered Pt₁₃H₂₆ clusters. These two clusters are regarded respectively as models in the absence or in the presence of a hydrogen pressure, as indicated above. Although H₂ is a product of the reaction, and hence always present, the influence of hydrogen coadsorbates is rarely considered in the modeling.⁷² Since the particle has a high H coverage, previous calculations have shown that it only develops a very weak interaction with the support,⁴² hence justifying the chosen approximation here of not considering the support influence in the simulations.

To determine the activity of the model catalysts for methane activation, the dissociation barrier of the first C–H bond is studied, since it is the rate-determining step on many catalysts.^{73–75} van der Waals interactions are important to describe the interaction between methane and the cluster and have been included by using the PBE-dDsC functional, which provides a posteriori correction to the PBE functional based on the electron density.^{76,77} The bare Pt₁₃ cluster is highly reactive for the C–H dissociation of methane, and the transition states share similar structures with an elongated C–H bonds coordinated on a single Pt atom (Table S6 in SI). Especially the GM0 of Pt₁₃ cluster (global minimum) readily dissociates methane with a barrier as small as 0.04 eV. Other metastable isomers are also very active for methane activation with a lowest barrier in the range 0.25–0.30 eV. This barrier is much smaller than the Pt(111) surface and Pt(211) edges (78.7 and 46.0 kJ/mol respectively).⁷⁸ The high activity of small bare Pt clusters toward alkane dehydrogenations has also been reported, as propane dehydrogenation on Pt₄.^{79,80} However, the bare Pt clusters or surfaces bind carbonaceous species very strongly and are not stable in reaction condition: they get deactivated by coke formation.

One way to prevent coking is to cofeed hydrogen with the alkane. Under a pressure of hydrogen, we have seen above that a high amount of H atoms covers the Pt₁₃ cluster, and that the exact coverage depends on the temperature and partial pressure. In the considered conditions ($T = 400$ °C, $p(\text{H}_2) = 0.5$ bar) the cluster is highly covered with H atoms (Pt₁₃H₂₆ cluster model) and one might wonder whether C–H activation is still possible with such a high H coverage. Since most of the surface sites on Pt₁₃H₂₆ are occupied by hydrogen atoms, there are very limited numbers of sites available for methane dehydrogenation. According to the number of hydrogen neighbors, the surface Pt atoms can be classified in 4 types: PtH2 (Pt with two H neighbors), PtH3, PtH4 and PtH5 (where top site of Pt is occupied) (Figure S17). Considering the stoichiometry, and the fact that most H atoms are in bridge sites (and hence shared by two Pt atoms) the most probable coordination on the Pt₁₃H₂₆ cluster is PtH4. For the global minimum (GM0) only PtH3 and PtH4 sites are available and

for the second metastable structure GM2, only PtH4 is available. GM1 has the special property to show a low-coordinated PtH2 site. The transition state structures for the C–H bond activation of methane have been systematically explored on the three most stable isomers of Pt₁₃H₂₆ and different surface sites have been considered. The activation energy for C–H dissociation are shown on Figure 7 for each

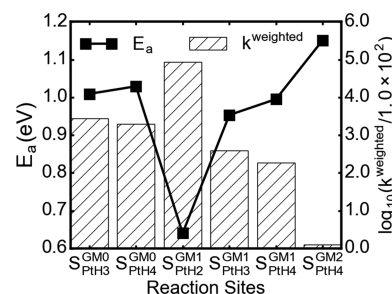


Figure 7. Methane activation on the Pt₁₃H₂₆ cluster. The activation energies (E_a (eV)) and the relative contribution to the reaction rate are shown for the global minimum (GM0) of the cluster and the first two metastable structures (GM1 and GM2). Pt sites with various H coordination are considered. The weighted reaction rate constant is given with a reference of 1×10^2 . The reaction temperature is chosen as 400 °C.

isomer and each type of surface site (the structure of the transition states is given in Figure S18 in SI). A strong dependence of the H coordination of the Pt site on its activity for methane dehydrogenation is found, the PtH2 site on the GM1 metastable isomer giving a lower barrier (~0.6 eV) compared to PtH3 or PtH4 sites (~1–1.1 eV). The reaction energy of the methane C–H cleavage is endothermic for all studied sites on the Pt₁₃H₂₆ cluster, but the PtH2 site on the first metastable isomer results in a much smaller endothermic character, its low coordination directly enabling to accommodate extra ligands from methane dissociation. The highest occupied and lowest unoccupied electronic states of the cluster show a larger contribution on PtH2 sites compared with PtH3, which also explains the higher activity (Figure S19) of PtH2 even though both of them have a vacancy site near the Pt atoms.

In analogy with the previous analysis for HER, we also normalized the rate constant of different isomers with their Boltzmann distribution:

$$k_s^{\text{weighted}} = A \exp\left(-\frac{E_a^{\text{GMi}}(S)}{k_B T}\right) \times \exp\left(-\frac{E^{\text{GMi}}(\text{cluster})}{k_B T}\right) \quad (8)$$

where $E^{\text{GMi}}(\text{cluster})$ is the energy of different cluster isomers. $E_a^{\text{GMi}}(S)$ is the barrier for methane dissociation reactions on GMi and on surface site S. Therefore, k_s^{weighted} considers both the stability and activity of different Pt₁₃H₂₆ isomers. It is striking that the first metastable isomer of Pt₁₃H₂₆ (GM1) dominates the total reaction rate, instead of the global minimum structure (Figure 7). The PtH2 site on GM1 is intrinsically 580 times more active than the best site on the global minimum, and even when correcting by its smaller presence probability, the metastable structure remains 30 times more active. Considering only the global minimum structure for the cluster would hence result in a marked underestimation of the overall reaction rate for methane dissociation.

This study on methane C–H activation on both Pt₁₃ and Pt₁₃H₂₆ clusters provides important insights about alkane dehydrogenation reactions on Pt nanocluster catalysts. On the bare cluster, in the absence of hydrogen, the initial conversion of alkanes is very high but the system is highly prone to coke formation and deactivation. If hydrogen is cofed with the alkane, the H covered Pt clusters are less active for methane dehydrogenations, but barriers remain reasonable despite the high H coverage. Activation barriers show a strong dependence on the H coordination of the Pt surface atom, being especially small if the H coordination of surface Pt is less or equal than 2. The C–H cleavage activity is hence strongly depending on the structure of the H adlayer. The first metastable structure shows one PtH₂ site and is hence much more reactive than the global minimum structure, where all surface Pt atoms have at least 3 H neighbors. The slightly endothermic reaction energy also implies that products are not easily further dehydrogenated, hence preventing coke formation and deactivation. On the modeling aspect, this example shows that it can be risky to consider only the global minimum structure for a cluster catalyst and that metastable structures can dominate the experimentally observed activity.

5. SUMMARY AND CONCLUSION

Uncovering the nature and structure of the site that performs the catalytic act, in the conditions of experimental catalysis, and understanding the origin of catalytic activity are ultimate targets for computational catalysis studies. Global optimization methods accompanied by first-principles thermodynamics are very successful in structure predictions, taking into account the presence of adsorbates at given temperature and gas pressure conditions. We show here that, in the case of nanosize Pt particles, considering the global minimum structure is not sufficient, but that low energy *metastable* isomers can contribute to or even dominate in the experimentally observed reaction activity (or selectivity). Cluster fluxionality, restructuring, dynamics and ensemble of metastable states hence play a key role. This brings the need for method to efficiently search for low energy isomers. A modified genetic algorithm (MGA) is proposed in this work, and the current approach has enabled us to comprehensively investigate the low energy metastable ensemble for bare and hydrogenated clusters catalytic reactions on clusters. The main idea that we are using a single parameter N_{wait} increasing of which could symmetrically improve the reliability and confidence of searching results. As far as we know, this proposed MGA is among the first attempts for systematically addressing metastable structures in catalysis research. Validation examples demonstrate the efficiency of this approach.

The global optimization methods take the advantages of a large number of structures optimizations, which are great challenges for DFT calculations. This is partially circumvented by exploiting a neural network potential. A final DFT refining is necessary in this work to get accurate prediction power, while this may prevent to use the current MGA approach for larger system. The use of DFT calculation could be dramatically reduced with more accurate NN potential, and this can be hopefully solved by exploiting more sophisticated NN implementations. Nevertheless, the proposed association of MGA and neural network accelerated structure exploration strategy is very important for future studies in the field of cluster catalysis, where the metastable isomers can play a major role in the experimentally observed reactivity.

The key importance of metastable structures in reaction conditions for catalytic reactivity, demonstrated here for nanosize Pt clusters under a pressure of hydrogen, is expected to extend to many other types of catalysts where a local rearrangement would create a slightly less stable but much more reactive site. This hence opens a new paradigm for catalysts design, by targeting not the most stable structure but the highly reactive low energy metastable isomers of the catalyst. The concept of metastability triggered surface reactivity could hence be central in catalysis, but also in corrosion science, growth and other surface related processes.

■ ASSOCIATED CONTENT

Supporting Information

The Supporting Information is available free of charge on the ACS Publications website at DOI: 10.1021/jacs.7b11239.

Section S1: details of density functional calculations; Section S2: details of frequency evaluation and free energy evaluation; Section S3: details of training HDNNP; Section S4: flowchart and validation of MGA; section S5: details of DFT results for HER and methane activation (PDF)

■ AUTHOR INFORMATION

Corresponding Author

*sautet@ucla.edu

ORCID

Philippe Sautet: 0000-0002-8444-3348

Notes

The authors declare no competing financial interest.

■ ACKNOWLEDGMENTS

This work used computational and storage services associated with the Hoffman2 Shared Cluster provided by UCLA Institute for Digital Research and Education's Research Technology Group. This work used the Extreme Science and Engineering Discovery Environment (XSEDE), which is supported by National Science Foundation grant number ACI-1548562.⁸¹ P. S. thanks UCLA for startup funding.

■ REFERENCES

- (1) Calle-Vallejo, F.; Tymoczko, J.; Colic, V.; Vu, Q. H.; Pohl, M. D.; Morgenstern, K.; Loffreda, D.; Sautet, P.; Schuhmann, W.; Bandarenka, A. S. *Science* **2015**, 350, 185–9.
- (2) Wang, X.; Tian, D. *Comput. Mater. Sci.* **2009**, 46, 239–244.
- (3) Huang, X.; Su, Y.; Sai, L.; Zhao, J.; Kumar, V. J. *Cluster Sci.* **2015**, 26, 389–409.
- (4) Vilhelmsen, L. B.; Hammer, B. *J. Chem. Phys.* **2014**, 141, 044711.
- (5) Lysgaard, S.; Myrdal, J. S.; Hansen, H. A.; Vegge, T. *Phys. Chem. Chem. Phys.* **2015**, 17, 28270–6.
- (6) Alexandrova, A. N. *J. Phys. Chem. A* **2010**, 114, 12591–12599.
- (7) Alexandrova, A. N.; Boldyrev, A. I.; Fu, Y. J.; Yang, X.; Wang, X. B.; Wang, L. S. *J. Chem. Phys.* **2004**, 121, 5709–19.
- (8) Wales, D. J.; Doye, J. P. K. *J. Phys. Chem. A* **1997**, 101, 5111–5116.
- (9) Wang, Y.; Lv, J.; Zhu, L.; Ma, Y. *Phys. Rev. B: Condens. Matter Mater. Phys.* **2010**, 82, 094116.
- (10) Duanmu, K.; Truhlar, D. G. *J. Phys. Chem. C* **2015**, 119, 9617–9626.
- (11) Zhai, H.; Ha, M. A.; Alexandrova, A. N. *J. Chem. Theory Comput.* **2015**, 11, 2385–93.
- (12) Reuter, K.; Scheffler, M. *Phys. Rev. B: Condens. Matter Mater. Phys.* **2001**, 65, 035406.

- (13) Reuter, K.; Scheffler, M. *Phys. Rev. B: Condens. Matter Mater. Phys.* **2003**, *68*, 045407.
- (14) Li, Z. H.; Truhlar, D. G. *Chem. Sci.* **2014**, *5*, 2605–2624.
- (15) Liu, J. X.; Su, H. Y.; Sun, D. P.; Zhang, B. Y.; Li, W. X. *J. Am. Chem. Soc.* **2013**, *135*, 16284–7.
- (16) Dobrushin, R. L.; Kotecký, R.; Shlosman, S. *Wulff Construction: A Global Shape from Local Interaction*; American Mathematical Society: Providence, RI, 1992; Vol. 104.
- (17) Handzlik, J.; Sautet, P. *J. Catal.* **2008**, *256*, 1–14.
- (18) Goldsmith, B. R.; Sanderson, E. D.; Bean, D.; Peters, B. J. *Chem. Phys.* **2013**, *138*, 204105.
- (19) Ha, M.-A.; Baxter, E. T.; Cass, A. C.; Anderson, S. L.; Alexandrova, A. N. *J. Am. Chem. Soc.* **2017**, *139*, 11568–11575.
- (20) Baxter, E. T.; Ha, M.-A.; Cass, A. C.; Alexandrova, A. N.; Anderson, S. L. *ACS Catal.* **2017**, *7*, 3322–3335.
- (21) Zhai, H.; Alexandrova, A. N. *ACS Catal.* **2017**, *7*, 1905–1911.
- (22) Oganov, A. R. *Modern Methods of Crystal Structure Prediction*; Wiley-VCH Verlag & Co. KGaA: Weinheim, 2010.
- (23) van Duin, A. C. T.; Dasgupta, S.; Lorant, F.; Goddard, W. A. *J. Phys. Chem. A* **2001**, *105*, 9396–9409.
- (24) Senfle, T. P.; Hong, S.; Islam, M. M.; Kylasa, S. B.; Zheng, Y.; Shin, Y. K.; Junkermeier, C.; Engel-Herbert, R.; Janik, M. J.; Aktulga, H. M.; Verstraelen, T.; Grama, A.; van Duin, A. C. T. *npj Comput. Mater.* **2016**, *2*, 15011.
- (25) Bartók, A. P.; Csányi, G. *Int. J. Quantum Chem.* **2015**, *115*, 1051–1057.
- (26) Behler, J. *Int. J. Quantum Chem.* **2015**, *115*, 1032–1050.
- (27) Behler, J. *J. Phys.: Condens. Matter* **2014**, *26*, 183001.
- (28) Behler, J. *J. Chem. Phys.* **2011**, *134*, 074106.
- (29) Artrith, N.; Urban, A. *Comput. Mater. Sci.* **2016**, *114*, 135–150.
- (30) Artrith, N.; Morawietz, T.; Behler, J. *Phys. Rev. B: Condens. Matter Mater. Phys.* **2011**, *83*, 153101.
- (31) Artrith, N.; Kolpak, A. M. *Comput. Mater. Sci.* **2015**, *110*, 20–28.
- (32) Artrith, N.; Hiller, B.; Behler, J. *Phys. Status Solidi B* **2013**, *250*, 1191–1203.
- (33) Behler, J.; Parrinello, M. *Phys. Rev. Lett.* **2007**, *98*, 146401.
- (34) Behler, J. *Angew. Chem., Int. Ed.* **2017**, *56*, 2–15.
- (35) Barião, O. A.; Holmen, A.; Blekkan, E. A. *J. Catal.* **1996**, *158*, 1–12.
- (36) Xu, W.-X.; Schierbaum, K. D.; Goepel, W. *Appl. Surf. Sci.* **1996**, *103*, 279–287.
- (37) Ackermann, M. D.; Pedersen, T. M.; Hendriksen, B. L.; Robach, O.; Bobaru, S. C.; Popa, I.; Quiros, C.; Kim, H.; Hammer, B.; Ferrer, S.; Frenken, J. W. *Phys. Rev. Lett.* **2005**, *95*, 255505.
- (38) Xu, Y.; Getman, R. B.; Shelton, W. A.; Schneider, W. F. *Phys. Chem. Chem. Phys.* **2008**, *10*, 6009–18.
- (39) Yang, M.-L.; Zhu, Y.-A.; Zhou, X.-G.; Sui, Z.-J.; Chen, D. *ACS Catal.* **2012**, *2*, 1247–1258.
- (40) Xu, H.; Zhang, M.; Chen, Y.; Liu, H.; Xu, K.; Huang, X. *Comput. Theor. Chem.* **2015**, *1061*, 52–59.
- (41) Lei, Y.; Jelic, J.; Nitsche, L. C.; Meyer, R.; Miller, J. *Top. Catal.* **2011**, *54*, 334–348.
- (42) Mager-Maury, C.; Bonnard, G.; Chizallet, C.; Sautet, P.; Raybaud, P. *ChemCatChem* **2011**, *3*, 200–207.
- (43) Nykänen, L.; Honkala, K. *J. Phys. Chem. C* **2011**, *115*, 9578–9586.
- (44) Artrith, N.; Kolpak, A. M. *Nano Lett.* **2014**, *14*, 2670–6.
- (45) Cubuk, E. D.; Malone, B. D.; Onat, B.; Waterland, A.; Kaxiras, E. *J. Chem. Phys.* **2017**, *147*, 024104.
- (46) Doye, J. P. K.; Miller, M. A.; Wales, D. J. *J. Chem. Phys.* **1999**, *111*, 8417–8428.
- (47) Gautier, S.; Steinmann, S. N.; Michel, C.; Fleurat-Lessard, P.; Sautet, P. *Phys. Chem. Chem. Phys.* **2015**, *17*, 28921–30.
- (48) Park, J.; Yu, B. D.; Hong, S. *Curr. Appl. Phys.* **2015**, *15*, 885–891.
- (49) Duanmu, K.; Truhlar, D. G. *J. Chem. Theory Comput.* **2017**, *13*, 835–842.
- (50) Zhang, M.; Fournier, R. *Phys. Rev. A: At., Mol., Opt. Phys.* **2009**, *79*, 043203.
- (51) Zhai, H.; Alexandrova, A. N. *J. Chem. Theory Comput.* **2016**, *12*, 6213–6226.
- (52) Bunău, O.; Bartolomé, J.; Bartolomé, F.; Garcia, L. M. *J. Phys.: Condens. Matter* **2014**, *26*, 196006.
- (53) Piotrowski, M. J.; Piquini, P.; Da Silva, J. L. F. *Phys. Rev. B: Condens. Matter Mater. Phys.* **2010**, *81*, 155446.
- (54) Paul, J.-F.; Sautet, P. *Phys. Rev. B: Condens. Matter Mater. Phys.* **1996**, *53*, 8015.
- (55) Blonski, P.; Dennler, S.; Hafner, J. *J. Chem. Phys.* **2011**, *134*, 034107.
- (56) Yuan, H. K.; Chen, H.; Kuang, A. L.; Wu, B. *J. Magn. Magn. Mater.* **2013**, *331*, 7–16.
- (57) Itoi, H.; Nishihara, H.; Kobayashi, S.; Ittisanronnachai, S.; Ishii, T.; Berenguer, R.; Ito, M.; Matsumura, D.; Kyotani, T. *J. Phys. Chem. C* **2017**, *121*, 7892–7902.
- (58) Shustorovich, E. *Adv. Catal.* **1990**, *37*, 101–163.
- (59) Reuter, K.; Scheffler, M. *Phys. Rev. Lett.* **2003**, *90*, 046103–046103.
- (60) Reuter, K.; Scheffler, M. *Phys. Rev. B: Condens. Matter Mater. Phys.* **2001**, *65*, 035406–035406.
- (61) Gautier, S.; Sautet, P. *J. Phys. Chem. C* **2017**, *121*, 25152–25163.
- (62) Nørskov, J. K.; Bligaard, T.; Logadottir, A.; Kitchin, J. R.; Chen, J. G.; Pandelov, S.; Stimming, U. *J. Electrochem. Soc.* **2005**, *152*, J23.
- (63) Nawaz, Z. *Rev. Chem. Eng.* **2015**, *31*, 413–436.
- (64) Zaera, F. *Catal. Lett.* **2003**, *91*, 1–10.
- (65) Nykänen, L.; Honkala, K. *ACS Catal.* **2013**, *3*, 3026–3030.
- (66) Bricker, J. C. *Top. Catal.* **2012**, *55*, 1309–1314.
- (67) Sattler, J. J. H. B.; Ruiz-Martinez, J.; Santillan-Jimenez, E.; Weckhuysen, B. M. *Chem. Rev.* **2014**, *114*, 10613–10653.
- (68) Galvita, V.; Siddiqi, G.; Sun, P.; Bell, A. T. *J. Catal.* **2010**, *271*, 209–219.
- (69) Sun, P.; Siddiqi, G.; Vining, W. C.; Chi, M.; Bell, A. T. *J. Catal.* **2011**, *282*, 165–174.
- (70) Sattler, J. J.; Beale, A. M.; Weckhuysen, B. M. *Phys. Chem. Chem. Phys.* **2013**, *15*, 12095–103.
- (71) Biloen, P.; Dautzenberg, F. M.; Sachtler, W. M. H. *J. Catal.* **1977**, *50*, 77–86.
- (72) Raybaud, P.; Chizallet, C.; Mager-Maury, C.; Digne, M.; Toulhoat, H.; Sautet, P. *J. Catal.* **2013**, *308*, 328–340.
- (73) Wang, C.-C.; Siao, S. S.; Jiang, J.-C. *J. Phys. Chem. C* **2012**, *116*, 6367–6370.
- (74) Shen, X.; Chen, J.; Zhang, Z.; Shao, K.; Zhang, D. H. *J. Chem. Phys.* **2015**, *143*, 144701.
- (75) Liang, Z.; Li, T.; Kim, M.; Asthagiri, A.; Weaver, J. F. *Science* **2017**, *356*, 299–303.
- (76) Steinmann, S. N.; Corminboeuf, C. *J. Chem. Phys.* **2011**, *134*, 044117.
- (77) Steinmann, S. N.; Corminboeuf, C. *J. Chem. Theory Comput.* **2011**, *7*, 3567–3577.
- (78) Migliorini, D.; Chadwick, H.; Nattino, F.; Gutiérrez-González, A.; Dombrowski, E.; High, E. A.; Guo, H.; Utz, A. L.; Jackson, B.; Beck, R. D. *J. Phys. Chem. Lett.* **2017**, *8*, 4177–4182.
- (79) Hauser, A. W.; Gomes, J.; Bajdich, M.; Head-Gordon, M.; Bell, A. T. *Phys. Chem. Chem. Phys.* **2013**, *15*, 20727–34.
- (80) Vajda, S.; Pellin, M. J.; Greeley, J. P.; Marshall, C. L.; Curtiss, L. A.; Ballentine, G. A.; Elam, J. W.; Catillon-Mucherie, S.; Redfern, P. C.; Mehmood, F.; Zapol, P. *Nat. Mater.* **2009**, *8*, 213–6.
- (81) Towns, J.; Cockerill, T.; Dahan, M.; Foster, I.; Gaither, K.; Grimshaw, A.; Hazlewood, V.; Lathrop, S.; Lifka, D.; Peterson, G. D.; Roskies, R.; Scott, J. R.; Wilkens-Diehr, N. *Comput. Sci. Eng.* **2014**, *16*, 62–74.